Phased Array Radio System Aided Inertial Navigation for Unmanned Aerial Vehicles

Sigurd M. Albrektsen
sigurd.albrektsen@ieee.org

Torleiv H. Bryne
torleiv.h.bryne@ieee.org

Tor A. Johansen
Centre for Autonomous Marine Operations and Systems (NTNU AMOS)
Department of Engineering Cybernetics
Norwegian University of Science and Technology
tor.arne.johansen@ntnu.no

***Abstract*—Two of the major challenges with beyond visual line of sight (BVLOS) operations for unmanned aerial vehicles (UAVs) today are navigation and communication. This paper presents a solution that takes on both problems simultaneously, using a phased array radio system (PARS) both for communication and to aid a micro-electro-mechanical inertial navigation system (INS), estimating position, velocity and attitude. The solution is independent of global navigation satellite system (GNSS) for positioning and highly resistant to malicious sources, such as spoofing and jamming.**

The state estimator presented in this paper fuses range and bearing measurements from the PARS with the measurements from an on-board inertial measurement unit, a magnetometer and a barometer. By aiding the INS with PARS position measurements, magnetometer readings and barometric measurements, drift-free PVA estimates are obtained. The PARS measurements can be used for navigation alongside today's GNSS solutions, or as a redundant backup system running in parallel.

To validate the observer, an experiment was carried out with a fixed wing UAV on an approximately 35 minute flight with a maximal distance of 5.35 km from the base station. During this flight a root-mean-square accuracy of 26.3 m compared to a real-time kinematic GNSS solution was achieved.

TABLE OF CONTENTS

This work was supported by the FRINATEK project "Low-Cost Integrated Navigation Systems Using Nonlinear Observer Theory" through the Norwegian Research Council, the MAROFF project "Hybrid Operations in Maritime Environments", the FRINATEK project "Multi-stage global stensor fusion for navigation" and the Centre of Autonomous Marine Operations and Systems (NTNU AMOS) at the Norwegian University of Science and Technology (NTNU), project numbers 221666, 269480, 250725 and 223254 respectively.

1. INTRODUCTION

Unmanned aerial vehicles' (UAVs) abilities to cover large distances in a short amount of time and their maneuverability, make them valuable as a mobile sensor platform in a multitude of both civilian and defense related applications. Especially in beyond visual line of sight (BVLOS) UAV flights, navigation and communication are highly important since the operator needs to know where the UAVs are, what they are sensing, and he or she needs to be able to send commands to the UAV.

The state of the art in GNSS-less navigation is to either use dead reckoning with inertial sensors, although the accuracy of the position estimates are rapidly deteriorating, or using camera vision solutions [1–8]. Camera systems have, however, several limitations. They are typically very computationally intensive and dependent on recognizing features. As feature detection is both surface and lighting dependent, some scenarios are not well suited for camera navigation. For example when flying over water, very few features are detectable.

Because of this, the state of the art in UAV navigation is that the navigation solution is critically dependent on global navigation satellite systems (GNSS), thus GNSS is a critical single point of failure (SPOF) for state of the art UAVs. As the GNSS signal has a very low signal-to-noise ratio, it is prone to disturbances from both malicious sources, such as jamming [9], spoofing [10] or selective availability (SA) [11]; and electromagnetic interference. Furthermore, both hardware and software errors within the GNSS receiver itself can occur. As UAV operations are emerging in both the civil and military sector, an absolute positioning system independent from GNSS for redundant navigation is an essential part of the UAV avionics.

In this paper a Phased Array Radio System (PARS) is used to provide absolute position measurements for navigation. To improve the accuracy of this navigation solution an inertial navigation system (INS) is used. The INS is used to improve the position estimates in-between the radio measurements, and to improve the bandwidth of the system. It can furthermore act as a smoothing filter on the position estimates with a large variance and it makes the attitude of the UAV observable when combined with a magnetometer. The INS is, however, only accurate in short time intervals as the measurements it provides are relative to the previously estimated state, and these errors accumulate with time.

Main contributions

This paper presents a navigation solution based on measurements from a Phased Array Radio System (PARS) along with an INS, a barometer and a magnetometer. By aiding a high-

bandwidth IMU with the absolute position measurements from a PARS, along with altitude measurements from a barometer and heading from a magnetometer, we achieve a high-bandwidth, drift-free navigation solution that is independent of GNSS. We test our filter in an experiment and compare the results to a real-time kinematics (RTK) GNSS solution. Compared to this solution we achieve a combined root-mean-square error of approximately $26.3\,\mathrm{m}$.

Paper overview

We start by introducing the phased array radio system in Section 2. Then we define the preliminaries in Section 3 before we introduce the necessary steps needed to use the PARS as a positioning system in Section 4. We continue with presenting our nonlinear observer for aided INS in Section 5. An experiment was carried out, and a description of the system and hardware used is described in Section 6. The results from this experiment are presented in Section 7 and a conclusion is given in Section 8, along with suggestions for future work.

2. PHASED ARRAY RADIO SYSTEM

Transmitting large amounts of data, for example when streaming high-resolution on-board camera images to a ground station, puts strict requirements on the available network transmission rates. With a phased array radio system (PARS) both the challenge of navigation and of communication is addressed with a single system. A PARS uses an array of antennas and electronic beamforming to direct the outgoing energy in a specified direction by altering the phase of the transmitted signal. Using this technique high transfer rates over long distances can be achieved. For example, the Radionor CRE2 achieves transfer rates of up to $15\,\mathrm{Mbit/s}$ at a distance of $20\,\mathrm{km}$, or $2.3\,\mathrm{Mbit/s}$ at $60\,\mathrm{km}$.

To be able to efficiently use electronic beamforming, the transmitting antenna needs to know the direction towards the receiving antenna. By first sending out a *ping* signal in all direction and then getting a response from the receiving antenna, the direction of the incoming radio waves can be estimated. This is done by accurately recording the time difference in when the signal is received by the different antennas, and then calculating the phase difference of the signal between each of the antennas. From these phase differences the bearing and elevation angles, denoted ψ_u and θ_u respectively, can be calculated. By additionally measuring the round-trip time of the signal, the range, denoted ρ_u, is measured. Thus can a PARS calculate the range, bearing and elevation, towards the UAV antenna in the ground-antennas coordinate system.

These position measurements enable either stand-alone positioning of the UAV, or PARS-based aiding of an inertial navigation system (INS) using range and bearing measurements obtained from the radio system. Due to the high transmission power and directionality of the PARS, these measurements are less susceptible to jamming compared to GNSS. In order to preserve the integrity of both the communication link and the positioning capabilities against malicious obstruction or tampering, the positioning data can be strongly encrypted before it is transmitted to the UAV. Hence, both the origin and integrity of the positioning solution are ensured. Another layer of security is implicitly added as only radios inside the visible sector of the ground radio are considered for the navigation solution, restricting the location of a malicious source.

Distance	Rate
$20\,\mathrm{km}$	$15\,\mathrm{Mbit/s}$
$30\,\mathrm{km}$	$7\,\mathrm{Mbit/s}$
$60\,\mathrm{km}$	$2.3\,\mathrm{Mbit/s}$

Table 1: Radionor CRE2 communication rates

A drawback with the PARS navigation system compared to GNSS, is that for the PARS positioning to work, radio line of sight is required. The ground antenna has a visible frustum of 90 degrees in both vertical and horizontal directions, and a specified maximal is in the range of tens of kilometers. One might, however, extend the operational area of the PARS by adding additional ground antennas.

A navigation solution using only the Radionor CRE2 system with a barometer has been previously published in [12].

3. PRELIMINARIES

Before presenting the PARS-based positioning, and the PARS-aided INS, we state some preliminaries.

Notation

The Euclidean vector norm is denoted $\|\cdot\|_2$. The $n\times n$ identity matrix is denoted $\boldsymbol{I}_n$. Moreover, the transpose of a vector or a matrix is denoted $(\cdot)^\intercal$. Coordinate frames are denoted with $\{\cdot\}$. $\boldsymbol{S}(\cdot) \in SS(3)$ represents the skew symmetric matrix such that $\boldsymbol{S}(\boldsymbol{z}_1)\boldsymbol{z}_2 = \boldsymbol{z}_1 \times \boldsymbol{z}_2$ for two vectors $\boldsymbol{z}_1, \boldsymbol{z}_2 \in \mathbb{R}^{\not\Vdash}$. In addition, $\boldsymbol{z}^a_{bc} \in \mathbb{R}^{\not\Vdash}$ denotes a vector $\boldsymbol{z}$, to frame $\{c\}$, relative $\{b\}$, decomposed in $\{a\}$. Moreover, $\otimes$ denotes the Hamiltonian quaternion product. Saturation is represented by $\mathrm{sat}_\star$, where the subscript indicates the saturation limit.

The rotation matrix, $\boldsymbol{R}^b_a \in SO(3)$, describes the rotation between two given frames $\{a\}$ and $\{b\}$. Equivalently, the rotation between $\{a\}$ and $\{b\}$ may be represented using the unit quaternion $\boldsymbol{q}^b_a = (s, \boldsymbol{r}^\intercal)^\intercal$ where $s \in \mathbb{R}^1$ is the real part of the quaternion and $\boldsymbol{r} \in \mathbb{R}^3$ is the vector part. In addition, the Euler angles (roll, pitch and yaw) are given as

$$\boldsymbol{\Theta} = (\phi, \quad \theta, \quad \psi)^\intercal . \tag{1}$$

Latitude and longitude on Earth is represented by $\mu \in [-\pi/2, \pi/2]$ and $\lambda \in (-\pi, \pi]$, respectively.

Coordinate Frames

This paper considers four coordinate frames; The Earth Centered Inertial (ECI) frame, the Earth Centered Earth Fixed (ECEF) frame, a tangent frame equivalent of an Earth-fixed North East Down (NED) frame, and the BODY reference frame, denoted $\{i\}$, $\{e\}$, $\{t\}$, and $\{b\}$, respectively (see Fig. 1). The NED directions are respectively denoted N, E, D.

Inertial Measurement Units

A simplified measurement model of an IMU, providing specific force and angular rate sensor (ARS) measurements, is given as

$$\boldsymbol{f}^b_{\mathrm{IMU}} = \boldsymbol{f}^b_{ib} + \boldsymbol{b}^b_{\mathrm{acc}} + \boldsymbol{w}^b_{\mathrm{acc}} \tag{2}$$

$$\boldsymbol{\omega}^b_{\mathrm{IMU}} = \boldsymbol{\omega}^b_{ib} + \boldsymbol{b}^b_{\mathrm{ars}} + \boldsymbol{w}^b_{\mathrm{ars}} \tag{3}$$

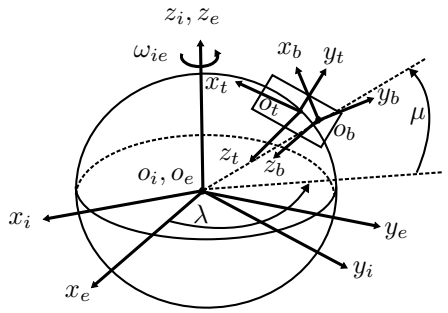

Figure 1: Definitions of the BODY, Tangent, ECEF and ECI reference frames.

where $\boldsymbol{f}_{ib}^b$ is the specific force, relating to the acceleration and gravity vector, $\boldsymbol{g}_b^t = (0, 0, g)^\intercal$ through

$$\begin{aligned}\boldsymbol{f}_{ib}^b &= \boldsymbol{R}_n^b \dot{\boldsymbol{v}}_{ib}^t - \boldsymbol{R}_t^b \boldsymbol{g}_b^t \\ &= \boldsymbol{a}_{ib}^b + \boldsymbol{S}(\boldsymbol{\omega}_{ib}^b)\boldsymbol{v}_{ib}^b - \boldsymbol{R}_t^b \boldsymbol{g}_b^t. \end{aligned} \tag{4}$$

$\boldsymbol{\omega}_{ib}^b$ represents angular velocity, while $\boldsymbol{v}_{ib}^b$, represents the BODY-fixed linear velocity. The BODY-fixed acceleration is represented by $\boldsymbol{a}_{ib}^b$, while $\boldsymbol{S}(\boldsymbol{\omega}_{ib}^b)\boldsymbol{v}_{ib}^b$ constitutes the centripetal accelerations. $\boldsymbol{b}_\star^b$ represent the accelerometer (acc) biases, and the angular rate sensor (ars) biases, respectively. $\boldsymbol{w}_\star^b$ represent noise.

Strapdown Equations

The NLO-based INS is derived using

$$\dot{\boldsymbol{p}}_{tb}^t = \boldsymbol{v}_{tb}^t \tag{5}$$

$$\dot{\boldsymbol{v}}_{tb}^t = -2\boldsymbol{S}(\boldsymbol{\omega}_{it}^t)\boldsymbol{v}_{tb}^t + \boldsymbol{R}_b^t \boldsymbol{f}_{ib}^b + \boldsymbol{g}_b^t \tag{6}$$

$$\dot{\boldsymbol{q}}_b^t = \frac{1}{2}\boldsymbol{q}_b^t \otimes \begin{pmatrix} 0 \\ \boldsymbol{\omega}_{ib}^b \end{pmatrix} - \frac{1}{2}\boldsymbol{q}_b^t \otimes \begin{pmatrix} 0 \\ \boldsymbol{\omega}_{it}^t \end{pmatrix} \tag{7}$$

as strapdown equations. Moreover,

$$\boldsymbol{\omega}_{it}^t = \boldsymbol{\omega}_{ie}^t = \begin{pmatrix} \cos(\mu) \\ 0 \\ -\sin(\lambda) \end{pmatrix} \omega_{ie}, \tag{8}$$

[13], due to $\{t\}$ being Earth fixed and thus $\boldsymbol{\omega}_{et}^t = \boldsymbol{0}_{3\times 1}$. $\boldsymbol{p}_{tb}^t$ and $\boldsymbol{v}_{tb}^t$ represents the position and velocity vectors, respectively.

4. Phased Array Radio System Positioning

As described in Section 1 the range, elevation and bearing from the ground antenna towards the UAV can be calculated by observing incoming signals from the UAV. To be able to use these measurements for navigation, they need to be rotated into the UAV's positional reference frame. To do this, the pose of the base station needs to be known.

PARS base station pose

To be able to use the PARS system for different experiments, a mobile PARS base station is used. A downside of this approach is that the pose of the base station needs to be calibrated on a per-mission basis. Although a rough estimate can done manually, an automatic calibration routine is advantageous, not only to save time, but also to increase the accuracy of the pose estimate.

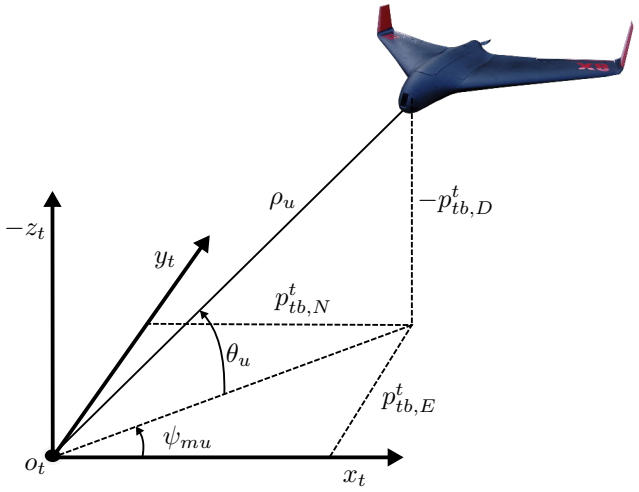

Figure 2: Range/bearing.

To ensure high-quality data for the base station pose estimation, missions can be preceded by a calibration phase, where the UAV is maneuvered in an area with good GNSS coverage and optimal visibility from the base station. From this data, an RTK solution can be calculated, and by using the position measurements from the PARS, the pose of the base station PARS can be estimated as described in [12].

Positioning: Range/bearing/elevation measurements—These PARS measurements can be utilized to calculate the relative position of the navigating craft in a local Earth-fixed frame, tangent frame is this paper, by relating the range/bearing measurements above to the UAV radio position, $\boldsymbol{p}_{\text{PARS}}^t$ using,

$$\begin{aligned}\rho_u &= \|\boldsymbol{p}_{\text{PARS}}^t\|_2 \\ &= \sqrt{\left(p_{tb,\text{N}}^t\right)^2 + \left(p_{tb,\text{E}}^t\right)^2 + \left(p_{tb,\text{D}}^t\right)^2}, \end{aligned} \tag{9}$$

$$\psi_u = \arctan\left(\frac{p_{tb,\text{E}}^t}{p_{tb,\text{N}}^t}\right), \tag{10}$$

$$\theta_u = \arctan\left(\frac{-p_{tb,\text{D}}^t}{\sqrt{(p_{tb,\text{N}}^t)^2 + (p_{tb,\text{E}}^t)^2}}\right). \tag{11}$$

These relationships are similar to those in [14, Ch. 13.6.2.2], used for radar tracking of aircraft, and can derived from

$$\boldsymbol{p}_{\text{PARS}}^t = \begin{pmatrix} p_{tb,\text{N}}^t \\ p_{tb,\text{E}}^t \\ p_{tb,\text{D}}^t \end{pmatrix} = \begin{pmatrix} \rho\cos(\psi_u)\cos(\theta_u) \\ \rho\sin(\psi_u)\cos(\theta_u) \\ -\rho\sin(\theta_u)) \end{pmatrix}. \tag{12}$$

according to Figure 2.

5. Nonlinear observer for aided INS

The UAS position, velocity and attitude (PVA) is estimated using a feedback-interconnected nonlinear observer integration strategy as depicted in Fig. 3, based on the work of

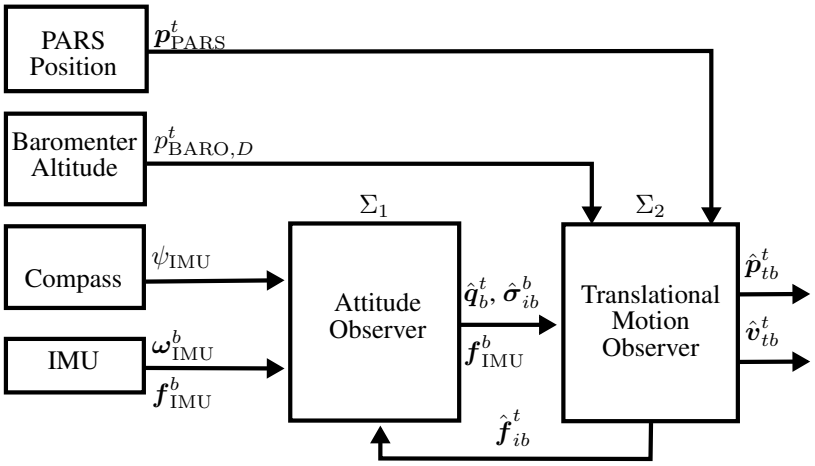

Figure 3: NLO structure overview

[15] and references therein. The PVA estimation is carried out in two steps. First the attitude is estimated by using rate gyro, specific force and heading reference measurements. The attitude observer is further aided by the second step, consisting of a Translational Motion Observer (TMO) providing specific force estimates in the navigation frame, together with 3-DOF position and velocity estimates based on the estimated attitude, in addition to, specific force, and aiding sensors.

Aiding Sensors

The aiding measurements in the attitude observer is the accelerometer used for leveling, and the UAVs autopilot compass, ψ_{auto}. Due to signal reflections in the ocean surface, the vertical accuracy of the PARS is reduced significantly. To compensate for this inaccuracy, the TMO is aided by a barometer in addition to using the horizontal PARS position obtained in section 4, motivated by [12].

Attitude Observer

The NLO for estimating the attitude between the $\{b\}$ and the $\{t\}$ frame is given similar to [15],

$$\Sigma_1 : \begin{cases} \dot{\hat{\boldsymbol{q}}}^t_b = \frac{1}{2}\hat{\boldsymbol{q}}^t_b \otimes \begin{pmatrix} 0 \\ \hat{\boldsymbol{\omega}}^b_{ib} \end{pmatrix} - \frac{1}{2}\begin{pmatrix} 0 \\ \boldsymbol{\omega}^t_{it} \end{pmatrix} \otimes \hat{\boldsymbol{q}}^t_b, & \text{(13a)} \\ \hat{\boldsymbol{\omega}}^b_{ib} = \boldsymbol{\omega}^b_{\mathrm{IMU}} - \hat{\boldsymbol{b}}^b_{\mathrm{ars}} + \hat{\boldsymbol{\sigma}}^b_{ib}, & \text{(13b)} \\ \dot{\hat{\boldsymbol{b}}}^b_{\mathrm{ars}} = \mathrm{Proj}\left(\hat{\boldsymbol{b}}^b_{\mathrm{ars}}, -k_I\hat{\boldsymbol{\sigma}}^b_{ib}\right), & \text{(13c)} \end{cases}$$

where $\mathrm{Proj}(\star,\star)$ denotes the angular rate bias projection algorithm ensuring that $\|\hat{\boldsymbol{b}}^b_{\mathrm{ars}}\|_2 \leq M_{\hat{b}_{\mathrm{ars}}}$ for $M_{\hat{b}_{\mathrm{ars}}} > M_{b_{\mathrm{ars}}}$ [16], and k_I is the gain associated with the rate gyro bias estimation. The NLO is structurally the same as in [15], where the attitude between the $\{b\}$ and the $\{e\}$ frame was estimated. Moreover, the observer's nonlinear injection term, $\hat{\boldsymbol{\sigma}}^b_{ib}$, is given as

$$\hat{\boldsymbol{\sigma}}^b_{ib} = k_1\underline{\boldsymbol{v}}^b_1 \times \boldsymbol{R}^{\intercal}(\hat{\boldsymbol{q}}^t_b)\underline{\boldsymbol{v}}^t_1 + k_2\underline{\boldsymbol{v}}^b_2 \times \boldsymbol{R}^{\intercal}(\hat{\boldsymbol{q}}^t_b)\underline{\boldsymbol{v}}^t_2, \qquad (14)$$

where the measurement vectors $\underline{\boldsymbol{v}}^b_{1,2}$ and reference vectors $\underline{\boldsymbol{v}}^t_{1,2}$ are calculated using

$$\underline{\boldsymbol{v}}^b_1 = \underline{\boldsymbol{f}}^b, \qquad \underline{\boldsymbol{v}}^t_1 = \underline{\boldsymbol{f}}^t, \qquad (15)$$

$$\underline{\boldsymbol{v}}^b_2 = \underline{\boldsymbol{f}}^b \times \underline{\boldsymbol{c}}^b, \quad \underline{\boldsymbol{v}}^t_2 = \underline{\boldsymbol{f}}^t \times \underline{\boldsymbol{c}}^t. \qquad (16)$$

Furthermore, the measurement and corresponding reference vector pairs in (15)–(16) are constructed as

$$\underline{\boldsymbol{f}}^b = \frac{\boldsymbol{f}^b_{\mathrm{IMU}}}{\|\boldsymbol{f}^b_{\mathrm{IMU}}\|_2}, \qquad \underline{\boldsymbol{f}}^t = \frac{\mathrm{sat}_{\mathrm{M_f}}(\hat{\boldsymbol{f}}^{\mathrm{t}}_{\mathrm{ib}})}{\|\mathrm{sat}_{\mathrm{M_f}}(\hat{\boldsymbol{f}}^{\mathrm{t}}_{\mathrm{ib}})\|_2}, \qquad (17)$$

$$\underline{\boldsymbol{c}}^b = \begin{pmatrix} \cos(\psi_{\mathrm{auto}}) \\ -\sin(\psi_{\mathrm{auto}}) \\ 0 \end{pmatrix}, \quad \underline{\boldsymbol{c}}^t = \begin{pmatrix} 1 \\ 0 \\ 0 \end{pmatrix}, \qquad (18)$$

where ψ_{auto} is a heading measurement provided from a given heading reference such as a compass or a attitude and heading reference system (AHRS). $\hat{\boldsymbol{f}}^t_{ib}$ is the estimated specific force, provided by the TMO, presented next in Sec. 5, as depicted in Fig. 3. The benefit of using normalized vectors is that the vector pairs only provide direction, hence these are dimensionless, such that the gains $k_{1,2}$ can be considered as cut-off frequencies of the complementary filter Σ_1, [17]. Since the gains have unit $\mathrm{rad/s}$, $\hat{\boldsymbol{\sigma}}^b_{ib}$ obtains the same unit as $\boldsymbol{\omega}^b_{\mathrm{IMU}}$.

Translational Motion Observer

The TMO is similar to that of [15], except that here the tangent frame is used as navigaiton frame, and given as follows,

$$\Sigma_2 : \begin{cases} \dot{\hat{\boldsymbol{p}}}^t_{tb} = \hat{\boldsymbol{v}}^t_{tb} + \vartheta\boldsymbol{K}^0_{pp}\tilde{\boldsymbol{y}}^t_{tb} & \text{(19a)} \\ \dot{\hat{\boldsymbol{v}}}^t_{tb} = -2\boldsymbol{S}(\boldsymbol{\omega}^t_{ie})\boldsymbol{v}^t_{tb} + \hat{\boldsymbol{f}}^t_{ib} + \boldsymbol{g}^t_b \\ \qquad + \vartheta^2\boldsymbol{K}^0_{vp}\tilde{\boldsymbol{y}}^t_{tb} & \text{(19b)} \\ \dot{\boldsymbol{\xi}}^t_{ib} = -\boldsymbol{R}(\hat{\boldsymbol{q}}^t_b)\boldsymbol{S}(\hat{\boldsymbol{\sigma}}^b_{ib})\boldsymbol{f}^b_{\mathrm{IMU}} \\ \qquad + \vartheta^3\boldsymbol{K}^0_{\xi p}\tilde{\boldsymbol{y}}^t_{tb} & \text{(19c)} \\ \hat{\boldsymbol{f}}^t_{ib} = \boldsymbol{R}(\hat{\boldsymbol{q}}^t_b)\boldsymbol{f}^b_{\mathrm{IMU}} + \boldsymbol{\xi}^t_{ib}, & \text{(19d)} \end{cases}$$

where

$$\tilde{\boldsymbol{y}}^t_{tb} = \begin{pmatrix} p^t_{\mathrm{PARS,N}} \\ p^t_{\mathrm{PARS,E}} \\ p^t_{\mathrm{BARO,D}} \end{pmatrix} - \hat{\boldsymbol{p}}^t, \qquad (20)$$

while $\boldsymbol{K}_\star$ are gains associated with the PARS and the barometer measurements. $\boldsymbol{\xi}^t_{ib}$ is an auxiliary state used to estimate $\boldsymbol{f}^t_{ib}$. ϑ is a high-gain like parameter used to guarantee

stability. Furthermore, by noting the linear time-varying (LTV) structure of (19) and defining

$$\boldsymbol{x} := \left(\boldsymbol{p}_{tb}^{t};\quad \boldsymbol{v}_{tb}^{t};\quad \boldsymbol{\xi}_{ib}^{t}\right), \tag{21}$$

the TMO can be written on LTV form as

$$\dot{\hat{\boldsymbol{x}}} = \boldsymbol{A}\hat{\boldsymbol{x}} + \boldsymbol{B}(t)\boldsymbol{u} + \boldsymbol{D}(t,\hat{\boldsymbol{x}}) + \boldsymbol{K}(t)(\boldsymbol{y} - \boldsymbol{C}\hat{\boldsymbol{x}}), \tag{22}$$

with the system matrices,

$$\boldsymbol{A} = \begin{pmatrix} \boldsymbol{0}_{3\times3} & \boldsymbol{I}_3 & \boldsymbol{0}_{3\times3} \\ \boldsymbol{0}_{3\times3} & \boldsymbol{0}_{3\times3} & \boldsymbol{I}_3 \\ \boldsymbol{0}_{3\times3} & \boldsymbol{0}_{3\times3} & \boldsymbol{0}_{3\times3} \end{pmatrix}, \boldsymbol{B}(t) = \begin{pmatrix} \boldsymbol{0}_{3\times3} & \boldsymbol{0}_{3\times3} \\ \boldsymbol{R}(\hat{\boldsymbol{q}}_b^t) & \boldsymbol{0}_{3\times3} \\ \boldsymbol{0}_{3\times3} & \boldsymbol{R}(\hat{\boldsymbol{q}}_b^t) \end{pmatrix}, \tag{23}$$

the measurement matrix,

$$\boldsymbol{C} = \begin{pmatrix} \boldsymbol{I}_3 & \boldsymbol{0}_{3\times3} & \boldsymbol{0}_{3\times3} \end{pmatrix}, \tag{24}$$

the vector,

$$\boldsymbol{D}(t,\hat{\boldsymbol{x}}) = \left(\boldsymbol{0}_{3\times1};\quad -2\boldsymbol{S}(\boldsymbol{\omega}_{ie}^{t})\hat{\boldsymbol{v}}_{tb}^{t} + \boldsymbol{g}_b^t;\quad \boldsymbol{0}_{3\times1}\right), \tag{25}$$

and the gain matrix,

$$\boldsymbol{K}(t) = \begin{pmatrix} \boldsymbol{K}_{pp} \\ \boldsymbol{K}_{vp} \\ \boldsymbol{K}_{\xi p} \end{pmatrix} = \begin{pmatrix} \vartheta \boldsymbol{K}_{pp}^{0} \\ \vartheta^2 \boldsymbol{K}_{vp}^{0} \\ \vartheta^3 \boldsymbol{K}_{\xi p}^{0} \end{pmatrix}, \tag{26}$$

where

$$\boldsymbol{K}^0(t) = \left((\boldsymbol{K}_{pp}^{0})^{\intercal} \quad (\boldsymbol{K}_{vp}^{0})^{\intercal} \quad (\boldsymbol{K}_{\xi p}^{0})^{\intercal}\right)^{\intercal} \tag{27}$$

is given obtain with $\boldsymbol{K}^0(t) = \boldsymbol{P}(t)\boldsymbol{C}^{\intercal}\boldsymbol{R}^{-1}(t)$, with $\boldsymbol{P}(t) = \boldsymbol{P}^{\intercal}(t) > 0$ being the solution of the time-scaled Riccati equation

$$\begin{aligned} \frac{1}{\vartheta}\dot{\boldsymbol{P}}(t) = \boldsymbol{A}\boldsymbol{P}(t) + \boldsymbol{P}(t)\boldsymbol{A}^{\intercal} - \boldsymbol{P}\boldsymbol{C}^{\intercal}\boldsymbol{R}^{-1}(t)\boldsymbol{C}^{\intercal}\boldsymbol{P}(t) \\ + \boldsymbol{B}(\hat{\boldsymbol{q}}_b^t)\boldsymbol{Q}(t)\boldsymbol{B}^{\intercal}(\hat{\boldsymbol{q}}_b^t). \end{aligned} \tag{28}$$

Finally, the input is given as

$$\boldsymbol{u} = \left(\boldsymbol{f}_{\text{IMU}}^{b}; -\boldsymbol{S}(\hat{\boldsymbol{\sigma}}_{ib}^{b})\boldsymbol{f}_{\text{IMU}}^{b}\right). \tag{29}$$

Moreover, the error states of the TMO can be defined as $\tilde{\boldsymbol{p}}_{tb}^{t} := \boldsymbol{p}_{tb}^{t} - \hat{\boldsymbol{p}}_{tb}^{t}$, $\tilde{\boldsymbol{v}}_{tb}^{t} := \boldsymbol{v}_{tb}^{t} - \hat{\boldsymbol{v}}_{tb}^{t}$, and $\tilde{\boldsymbol{f}}_{tb}^{t} := \boldsymbol{f}_{ib}^{t} - \hat{\boldsymbol{f}}_{ib}^{t}$, where the latter is obtained through a combination of (19c)–(19d), the resulting the error state is obtained,

$$\tilde{\boldsymbol{x}} := \left(\tilde{\boldsymbol{p}}_{tb}^{t};\quad \tilde{\boldsymbol{v}}_{tb}^{t};\quad \tilde{\boldsymbol{f}}_{ib}^{t}\right). \tag{30}$$

The corresponding error dynamics of the origin of Σ_2 is then obtained as

$$\dot{\tilde{\boldsymbol{x}}} = (\boldsymbol{A} - \boldsymbol{K}(t)\boldsymbol{C})\tilde{\boldsymbol{x}} + \boldsymbol{\rho}_1(t,\tilde{\boldsymbol{x}}) + \boldsymbol{\rho}_2(t,\boldsymbol{\chi}), \tag{31}$$

with

$$\boldsymbol{\rho}_1(t,\tilde{\boldsymbol{x}}) = \left(\boldsymbol{0}_{3\times1};\quad -2\boldsymbol{S}(\boldsymbol{\omega}_{ie}^{t})\tilde{\boldsymbol{v}}_{tb}^{t};\quad \boldsymbol{0}_{3\times1}\right), \tag{32}$$

$$\boldsymbol{\rho}_2(t,\boldsymbol{\chi}) = \left(\boldsymbol{0}_{3\times1};\quad \boldsymbol{0}_{3\times1};\quad \tilde{\boldsymbol{d}}(t,\boldsymbol{\chi})\right), \tag{33}$$

and where,

$$\begin{aligned} \tilde{\boldsymbol{d}}(t,\boldsymbol{\chi}) = (\boldsymbol{I}_3 - \boldsymbol{R}(\tilde{\boldsymbol{q}})^{\intercal})\,\boldsymbol{R}_b^t\left(\boldsymbol{S}(\boldsymbol{\omega}_{ib}^{b})\boldsymbol{f}_{ib}^{b} + \dot{\boldsymbol{f}}_{ib}^{b}\right) \\ - \boldsymbol{S}(\boldsymbol{\omega}_{it}^{t})\,(\boldsymbol{I}_3 - \boldsymbol{R}^{\intercal}(\tilde{\boldsymbol{q}}))\,\boldsymbol{R}_b^t\boldsymbol{f}_{ib}^{b} - \boldsymbol{R}^{\intercal}(\tilde{\boldsymbol{q}})\boldsymbol{R}_b^t\boldsymbol{S}(\tilde{\boldsymbol{b}}_{\text{ars}}^{b})\boldsymbol{f}_{ib}^{b}, \end{aligned} \tag{34}$$

similar to [15] and [18]. Hence, semiglobal exponential stability properties can be achieved as in the cited works.

6. Full-scale Test Setup

To verify the nonlinear observer with positional measurements from the PARS, an experiment was carried out using a Skywalker X8 UAV at Agdenes outside Trondheim, Norway on June 23rd 2016 in good weather conditions and a forecasted wind of 15 km/h. A ground track of the flight is given in Figure 4.

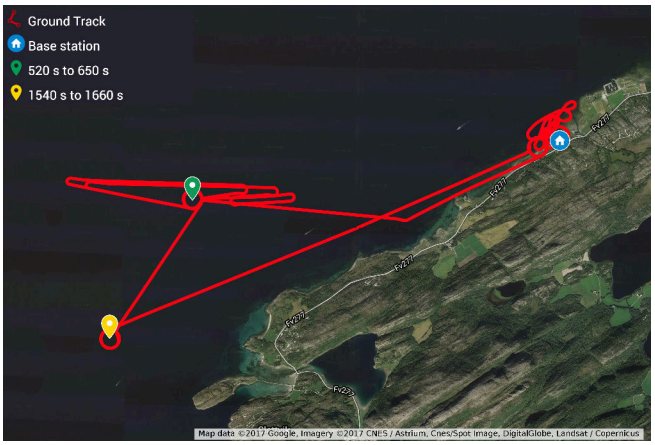

Figure 4: A map of the ground track of the flight. The green and yellow indicators are placed to indicate times when the UAV is loitering in circles. The building icon indicates the position of the ground station with the ground radio.

An overview of the experimental setup is given in Figure 6. The ground station consists of a Radionor Communications CRE2 189 PARS ground radio, a base station computer and an RTK GNSS receiver. The RTK GNSS receiver is needed to provide a high-quality RTK solution, which is used as a ground-truth for the navigation solution. The ground computer analyzes the direction of the received signals, and stores all the data logged by the ground system. This computer can also be used to configure and supervise the payload on-board the UAV during missions.

On-board the UAV, the payload is split into three parts; the on-board PARS, the experimental navigation stack, and the flight-critical avionics. This division is done to be able to easily move subsystems between different platforms, and the division is based on functionality: the PARS' primary function is to provide a communication link between the ground and the UAV payload, the navigation stack is responsible for providing a high-quality navigation solution for the UAV, and the avionics is responsible for all flight-critical functionality.

The on-board PARS is a Radionor Communications CRE2 144-LW and it allows encrypted communication with the navigation stack on-board the UAV from the ground station. The CRE2-144-LW weighs 85 g has dimensions of 120 mm x 65 mm x 13.3 mm, and uses AES-256 encryption. It is depicted in Figure 5. The navigation stack consists of a Hardkernel Odroid XU4 [19] on-board computer, with a SenTiBoard (previously named SyncBoard [20]) hardware synchronization board. The SenTiBoard reads and accurately records the timestamps of the incoming messages from a STIM 300 IMU [21] and a u-blox LEA-M8T GNSS receiver [22]. We use a PIXHAWK autopilot [23] with a 3DR GPS module containing a u-blox NEO-7N GPS receiver [24] and a Honeywell HMC5883L digital compass [25]. The barometer used in this paper is the PIXHAWK's integrated MEAS MS5611 [26].

For convenience, the data from the autopilot and navigation stack are synchronized using the GPS-time timestamps. To truly be able to operate without GPS coverage, this synchronization is not feasible, but receiving barometer and magnetometer data from the either from the autopilot's communication interface or through additional, external sensors is a trivial alteration.

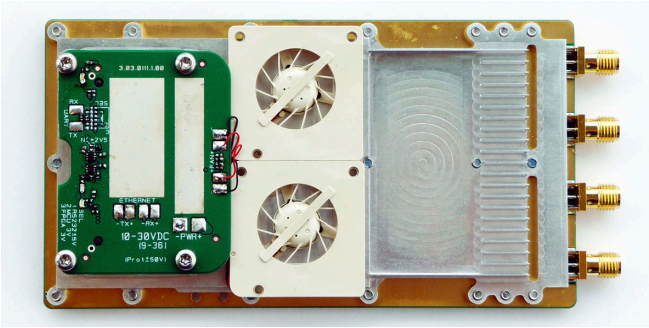

Figure 5: The Radionor CRE2 144-LW PARS

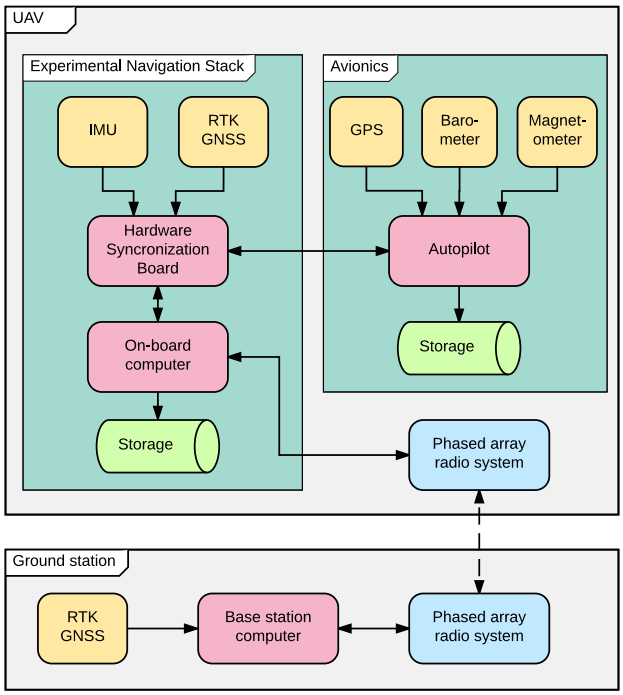

Figure 6: Overview of the UAV and ground station systems used in experiments. The dashed line between the radios represents wireless communication. For clarity, some components of the avionics are not shown in this overview.

7. Results

Reference measurements

To evaluate the performance of the position estimates from the PARS aided NLO, an RTK GNSS solution was calculated. This solution has centimeter-level accuracy, which is sufficient to be considered a ground-truth when compared to the PARS NLO. The RTK GNSS solution is denoted as *RTK GNSS* in the figures, and is shown with a green line.

The performance of the attitude observer is compared to the on-board autopilot's (the Pixhawk's) AHRS. Although the Pixhawk uses relatively low-cost sensors, it is well-tested, and provides an attitude solution which is independent from the PARS NLO. Note that this solution is not sufficiently accurate to be considered a ground truth, and we cannot say if the AHRS or the NLO performs better, but it should at least show the trends of the system. The Pixhawk's AHRS solution is denoted as *Pixhawk AHRS* in the figures, and is shown with a green line.

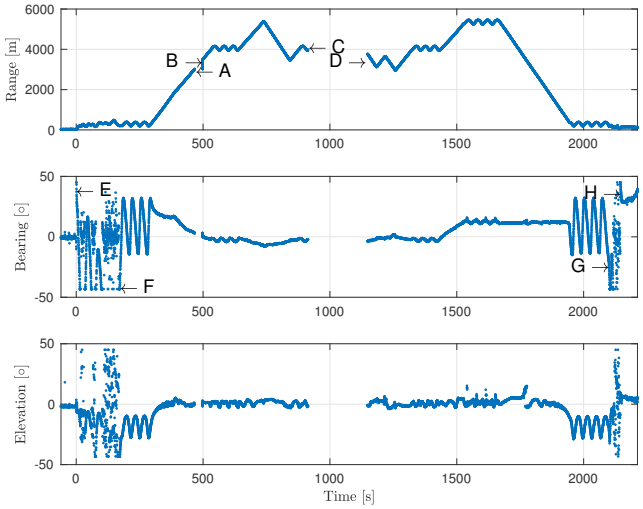

Figure 7: Raw PARS measurements.

Performance metrics

The results statistics presented in this paper is based on three performance metrics:

- Absolute Mean Error (AME),
- Standard Deviation (STD) and,
- Root-mean square (RMS) error

Raw PARS measurements

The raw range, bearing and elevation measurements are shown in Figure 7. Two file transfers disrupted the position measurements from 466 s - 498 s and 913 s - 1145 s, annotated in Figure 7 as A - B and C - D respectively. During the period from 0 s - 172 s, annotated as E - F, the UAV is circling near the ground antenna to ascend to cruising altitude. This causes the UAV to enter and exit the visible sector of the ground antenna, and when the UAV is outside this sector, the positioning does not work correctly. During the period from 2100 s - 2147 s, annotated as G - H, the UAV is landing and is also outside the visible sector of the UAV.

Results: Aided INS

To compare the effect of the feedback-interconnection described in Section 5, two versions of the NLO were realized: one with feedback-interconnection turned on, and one with feedback-interconnection turned off. Both the observers were tuned equally. The gains for the NLO were chosen as $k_1 = 0.095$, $k_2 = 0.6$, and $k_I = 0.0007$, and the TMO was tuned as follows:

$$\boldsymbol{R}_{\text{PARS}} = diag\left(7^2, 7^2, 0.0632^2\right),$$
$$\boldsymbol{Q}_{\text{PARS}} = diag\left(0.0308^2 \cdot \boldsymbol{I}_3, 50 \cdot \boldsymbol{I}_3\right).$$

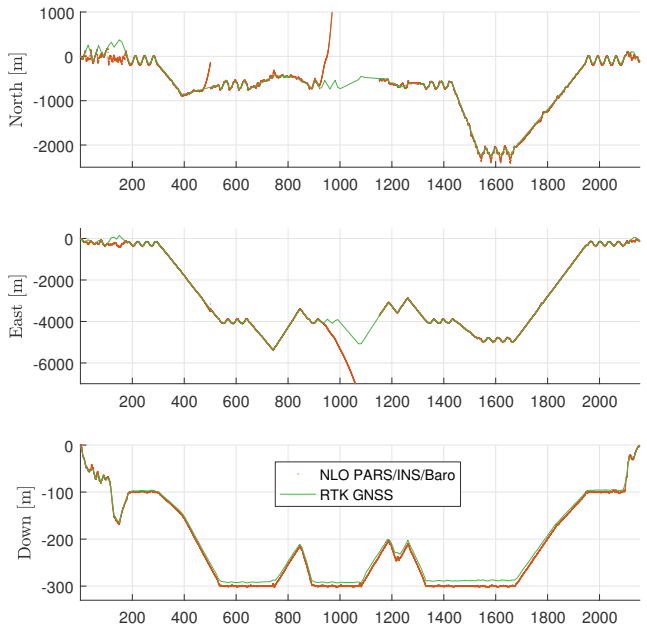

Figure 8: Position solution from NLO (with feedback interconnection).

Table 2: PARS/BARO/INS (with feedback interconnection): Error statistics relative relative RTK and Pixhawk

	North [m]	**East [m]**	**Down [m]**
AME:	16.78	6.86	7.17
STD:	23.34	9.00	3.56
RMS:	23.35	9.22	7.97
	Roll [deg]	**Pitch [deg]**	**Yaw [deg]**
AME:	2.67	2.70	1.98
STD:	4.02	4.04	3.41
RMS:	4.03	4.09	3.41

As position measurements are missing in the intervals from 466 s to 498 s and 913 s to 1145 s, the filters rapidly drift off during these intervals, as they rely only on dead reckoning, which the observer is not tuned to handle. These intervals heavily skew the metrics for accuracy, and to the better represent the performance of the PARS, the results presented are filtered to exclude these intervals. The estimates are still used internally in the filter, but the intervals are removed from the statistics in Tables 2 to 3 and the plots in Figure 12.

As can be seen when comparing Figure 9 to Figure 10, the NLO solution without feedback interconnection give better results when there are no position measurements from the radio. This is expected as the feedback interconnection is more sensitive to loss of the aiding sensor. To compensate for this, an improvement was made to the filter, where it turns off the feedback interconnection if there has not been any position measurements in a certain amount of time (set to 1 s in these results).

For this experiment we only had access to a single ground antenna, and limited options for antenna positioning. Due to

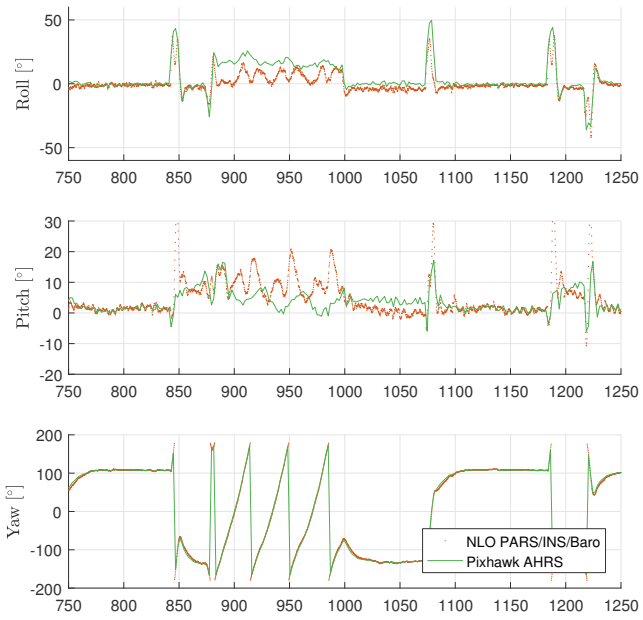

Figure 9: Attitude solution from NLO without feedback interconnection (position measurements missing from 913 s to 1145 s)

Table 3: PARS/BARO/INS (no feedback interconnection): Error statistics relative RTK and Pixhawk

	North [m]	**East [m]**	**Down [m]**
AME:	16.76	7.59	7.18
STD:	23.28	9.53	3.56
RMS:	23.29	9.81	7.97
	Roll [deg]	**Pitch [deg]**	**Yaw [deg]**
AME:	6.33	4.33	1.99
STD:	6.88	6.00	3.33
RMS:	8.69	6.25	3.33

these limitations we could not cover the whole area of the mission, particularly around the take-off and landing areas. In the following statistics the period when the UAV was outside the visible frustum of the ground antenna are omitted to represent a more realistic performance of the system.

From the comparisons given in Figure 12, and by comparing tables 2 and 3, we can see that the feedback interconnection does not significantly alter the performance of the position estimates, even when omitting the dead-reckoning parts of the flights. We see, however, that the estimates of both the pitch and roll are significantly improved by the feedback interconnection.

The velocity solution from the nonlinear observer and the Pixhawk's internal extended Kalman filter is shown in Figure 13.

8. Summary

The nonlinear observer presented in this paper fuses range and bearing measurements from the PARS with the mea-

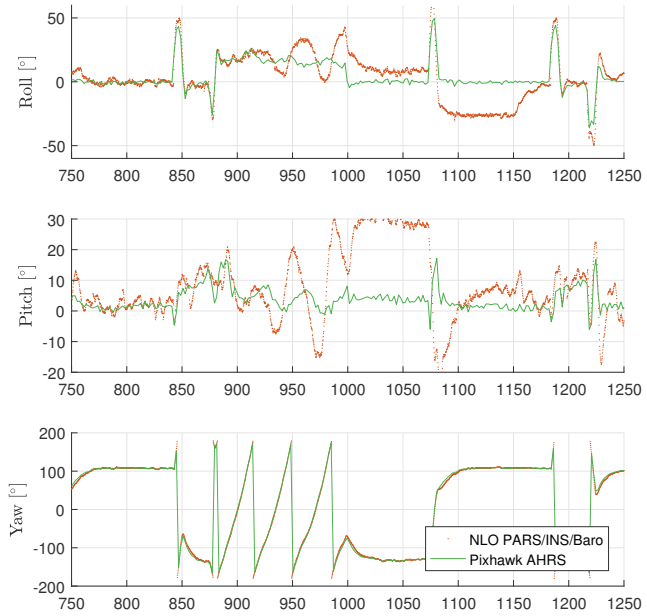

Figure 10: Attitude solution from NLO with feedback interconnection (position measurements missing from 913 s to 1145 s)

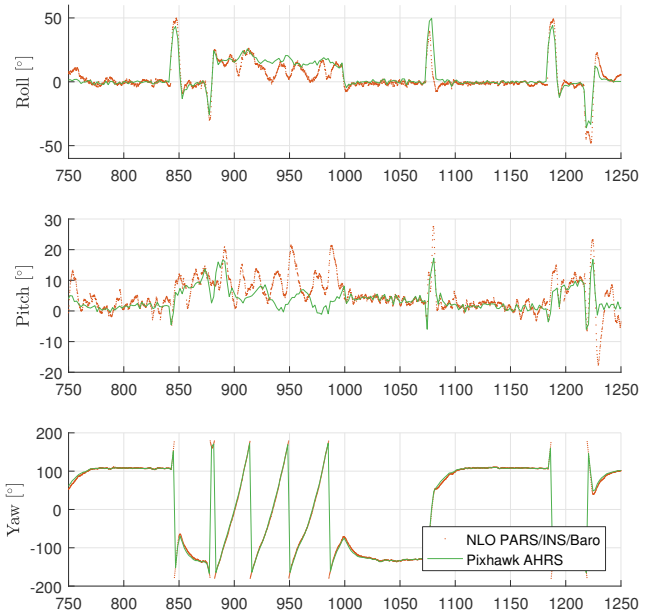

Figure 11: Attitude solution from NLO with thresholded feedback interconnection (position measurements missing from 913 s to 1145 s)

surements from the on-board inertial measurement unit, a magnetometer and a barometer. By aiding the INS with PARS measurements, compass readings, and altitude readings from a barometer, drift-free position, velocity and attitude estimates are obtained. In addition, the PARS measurements can be used for positioning alongside today's GNSS solutions, or as a redundant backup system running in parallel.

We have verified the performance of the PARS aided navigation filter through a BVLOS test experiment, by comparing the estimated position from the PARS aided navigation filter with real-time kinematic GNSS solution. The estimated attitude was compared with the autopilot's attitude estimates.

Compared to the RTK GNSS solution, we achieved an accuracy of approximately $26.3\,\mathrm{m}$ RMS on a flight with a maximal distance of $5.35\,\mathrm{km}$ from the ground station. Compared to the Pixhawk autopilot's AHRS solution, RMS attitude accuracy of approximately $4.0°$, $4.1°$ and $3.4°$ were achieved in roll, pitch and yaw respectively.

Further work

Although this implementation shows promising initial results, we expect that a tightly coupled observer will yield higher accuracy in both the position and attitude estimates.

This implementation assumes that the Earth is flat, which is an assumption that is accurate when covering small areas. When covering larger distances, however, this inaccuracy increases. We want to adapt the filter to handle a non-flat Earth model, to compare the effect of using different models when flying missions of tens of kilometers.

To be able to rely on the vertical component of the radio measurements, the accuracy needs to be improved significantly. We want to investigate if the error in the vertical direction is due to reflections by the ocean surface, and that both the real ranging signal and the reflected signals are detectable. If this is the case the detection algorithm can be altered to provide one or more alternative measurements, instead of only the best-guess of the signal. With such an alteration, techniques such as Multiple Hypothesis Tracking (MHT) can be used to make sure that the real signal is correctly tracked by the navigation system. If this system is implemented, the filter presented in this paper would no longer be reliant on the barometer.

Furthermore we want to perform more flights with longer ranges, and a hand-over scenario were several radios are used to increase the operational area of the system.

Acknowledgments

The authors thank Atle Sægrov, Tor Berg and Inge Aune Paulsen at Radionor Communications for their assistance with the phased array radio system, and our pilots Pål Kvaløy and Lars Semb at NTNU, and Carl Erik Stephansen and Torbjørn Houge at Maritime Robotics. We are also thankful for the help in the construction and testing of the UAV payload provided by the rest of the UAV team at NTNU, in particular Jakob M. Hansen, Kasper T. Borup, Lorenzo Fusini, Artur P. Zolich and Robert H. Rogne.

References

[1] J. Hardy, J. Strader, J. N. Gross, Y. Gu, M. Keck, J. Douglas, and C. N. Taylor, "Unmanned aerial vehicle relative navigation in GPS denied environments," in *2016 IEEE/ION Position, Location and Navigation Symposium (PLANS)*, April 2016, pp. 344–352.

[2] A. Bachrach, S. Prentice, R. He, and N. Roy, "RANGE–robust autonomous navigation in GPS-denied environments," *Journal of Field Robotics*, vol. 28, no. 5, pp. 644–666, 2011.

[3] T. Krajník, M. Nitsche, S. Pedre, L. Přeučil, and M. E. Mejail, "A simple visual navigation system for an

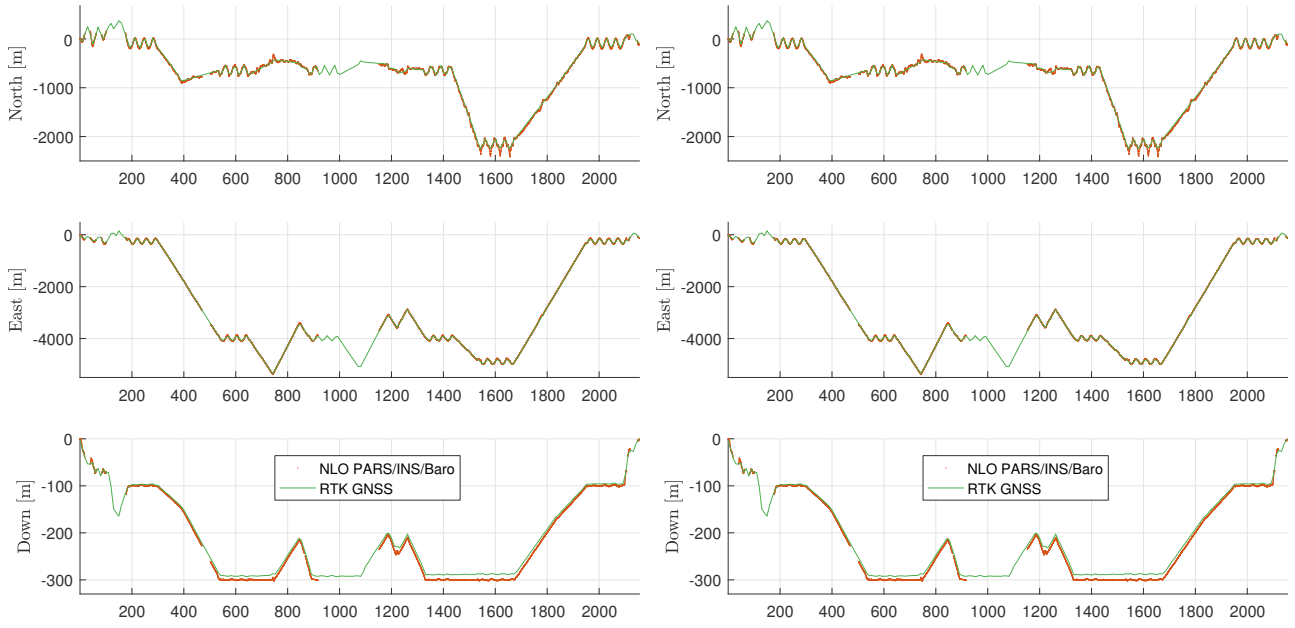

(a) Position estimate with no feedback interconnection

(b) Position estimates with feedback interconnection

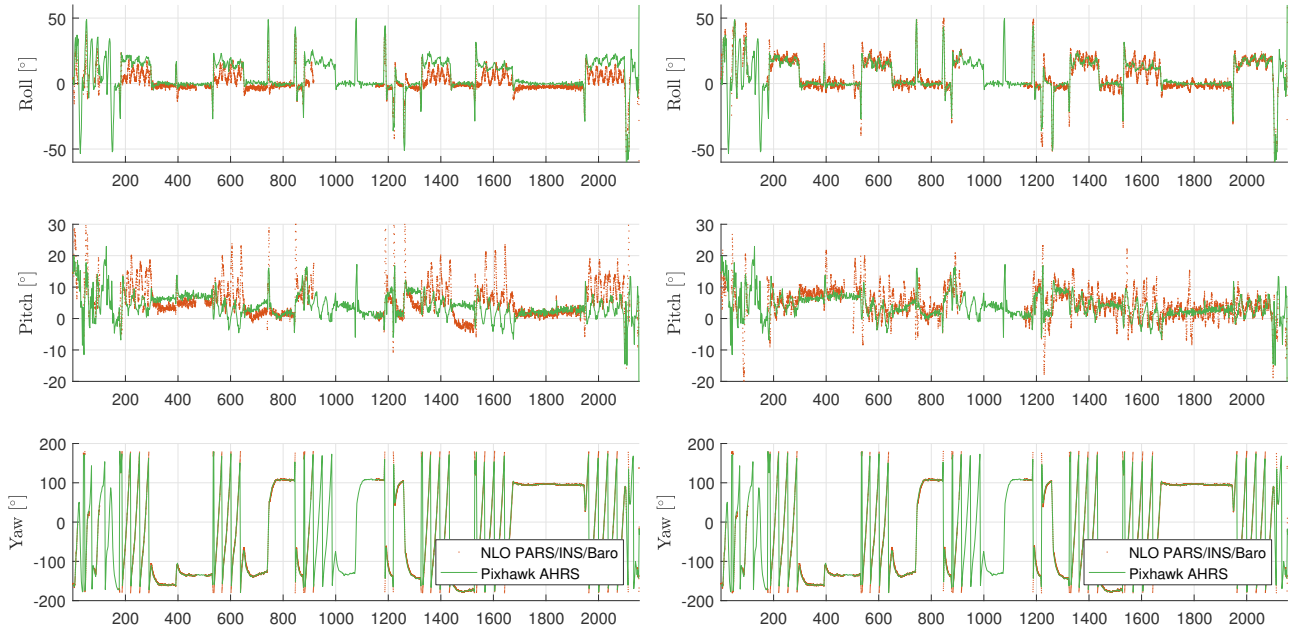

(c) Attitude with no feedback interconnection

(d) Attitude with feedback interconnection

Figure 12: Comparison of RTK GPS with position estimates from the NLO and attitude estimates, with and without feedback interconnection. The results are filtered to exclude the periods without radio position estimates and the periods when the UAV is outside the visible region of the radio antenna.

UAV," in *International Multi-Conference on Systems, Sygnals Devices*, March 2012, pp. 1–6.

[4] C. Liu, J. Nash, and S. Prior, "A low-cost vision-based unmanned aerial system for extremely low-light GPS-denied navigation and thermal imaging," *International Journal of Mechanical, Aerospace, Industrial, Mechatronic and Manufacturing Engineering*, vol. 9, no. 10, pp. 1750–1757, October 2015. [Online]. Available: https://eprints.soton.ac.uk/399629/

[5] S. Mishra and S. Saripalli, *GPS-free navigation for micro aerial vehicles*. American Helicopter Society International, 2015, pp. 189–193.

[6] L. Fusini, T. A. Johansen, and T. I. Fossen, "Dead reckoning of a fixed-wing UAV with inertial navigation aided by optical flow," in *2017 International Conference on Unmanned Aircraft Systems (ICUAS)*, June 2017, pp. 1520–1259.

[7] F. Kendoul and K. Nonami, "A visual navigation system for autonomous flight of micro air vehicles," in *2009 IEEE/RSJ International Conference on Intelligent*

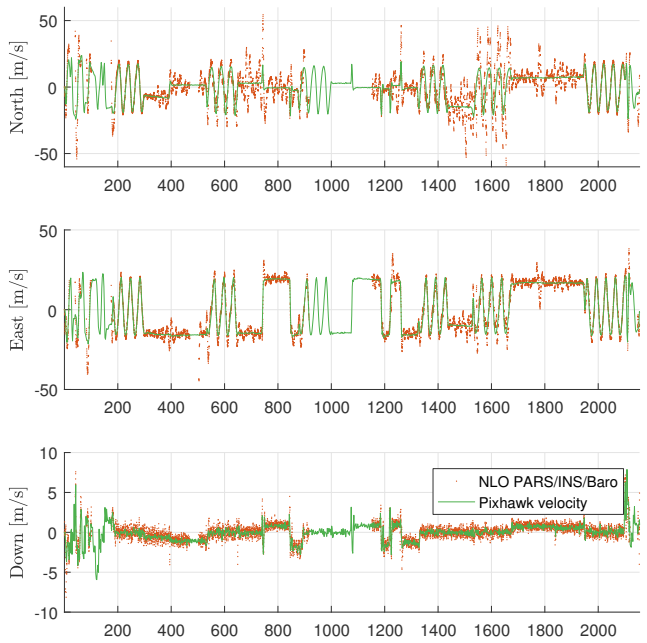

Figure 13: Velocity solution from NLO with feedback interconnection

Robots and Systems, Oct 2009, pp. 3888–3893.

[8] S. Weiss, R. Brockers, S. Albrektsen, and L. Matthies, "Inertial optical flow for throw-and-go micro air vehicles," in *2015 IEEE Winter Conference on Applications of Computer Vision*, Jan 2015, pp. 262–269.

[9] A. Pinker and C. Smith, "Vulnerability of the GPS signal to jamming," *GPS Solutions*, vol. 3, no. 2, pp. 19–27, 1999.

[10] A. J. Kerns, D. P. Shepard, J. A. Bhatti, and T. E. Humphreys, "Unmanned aircraft capture and control via GPS spoofing," *Journal of Field Robotics*, vol. 31, no. 4, pp. 617–636, 2014.

[11] G. T. Kremer, R. M. Kalafus, P. V. W. Loomis, and J. C. Reynolds, "The effect of selective availability on differential GPS corrections," *Navigation*, vol. 37, no. 1, pp. 39–52, 1990. [Online]. Available: http://dx.doi.org/10.1002/j.2161-4296.1990.tb01533.x

[12] S. M. Albrektsen, A. Sægrov, and T. A. Johansen, "Navigation of UAV using phased array radio," in *Workshop on Research, Education and Development of Unmanned Aerial Systems (RED UAS)*, 2017.

[13] J. A. Farrell, *Aided Navigation: GPS with High Rate Sensors*. McGraw-Hill, 2008.

[14] D. H. Titterton and J. L. Weston, *Strapdown inertial navigation technology*, 2nd ed. Institution of Electrical Engineers and American Institute of Aeronautics and Astronautics, 2004.

[15] H. F. Grip, T. I. Fossen, T. A. Johansen, and A. Saberi, "Nonlinear observer for GNSS-aided inertial navigation with quaternion-based attitude estimation," in *Proc. of the American Contr. Conf.*, Washington, DC, June 2013, pp. 272–279.

[16] ——, "Attitude estimation using biased gyro and vector measurements with time-varying reference vectors," *IEEE Transactions on Automatic Control*, vol. 57, no. 5, pp. 1332—1338, 2012.

[17] M.-D. Hua, G. Ducard, T. Hamel, R. Mahony, and K. Rudin, "Implementation of a nonlinear attitude estimator for aerial robotic vehicles," *IEEE Transactions On Control System Technology*, vol. 22, no. 1, pp. 201–212, 2014.

[18] T. A. Johansen, J. M. Hansen, and T. I. Fossen, "Nonlinear observer for tightly integrated inertial navigation aided by pseudo-range measurements," *ASME Journal of Dynamic Systems, Measurement and Control*, vol. 139, no. 1, pp. 011 007–011 007–10, 2017.

[19] *User Manual ODROID-XU4*, Hard Kernel, 2015. [Online]. Available: https://magazine.odroid.com/odroid-xu4

[20] S. M. Albrektsen and T. A. Johansen, "SyncBoard - a high accuracy sensor timing board for UAV payloads," in *2017 International Conference on Unmanned Aircraft Systems (ICUAS)*, June 2017, pp. 1706–1715.

[21] *STIM300 Inertia Measurement Unit*, sensonor, Apr. 2013, rev. 8. [Online]. Available: http://www.sensonor.com/media/91313/ts1524.r8%20datasheet%20stim300.pdf

[22] *u-blox 8 / u-blox M8 Receiver Description*, u-blox, May 2016, r11. [Online]. Available: https://www.u-blox.com/sites/default/files/products/documents/u-blox8-M8_ReceiverDescrProtSpec_%28UBX-13003221%29_Public.pdf

[23] L. Meier, D. Honegger, and M. Pollefeys, "PX4: A node-based multithreaded open source robotics framework for deeply embedded platforms," in *2015 IEEE International Conference on Robotics and Automation (ICRA)*, may 2015.

[24] *NEO-7 u-blox 7 GNSS modules*, u-blox, Nov. 2014, r07. [Online]. Available: https://www.u-blox.com/sites/default/files/products/documents/NEO-7_DataSheet_%28UBX-13003830%29.pdf

[25] *3-Axis Digital Compass IC HMC5883L*, Honeywell, 2 2013, rev. E.

[26] *MS5611-01BA03 Barometric Pressure Sensor*, Measurement Specialties, 9 2015.

BIOGRAPHY

Sigurd M. Albrektsen *received his M. Sc. degree in 2011 in Embedded Systems from the department of Engineering Cybernetics at the Norwegian University of Science and Technology (NTNU), Trondheim, Norway. In 2011 he started working at SINTEF as a research scientist in engineering cybernetics, where he is still employed. In 2014 he started working as a PhD candidate at NTNU, working with handling loss of GNSS positioning during beyond-visual-line-of-sight UAV flights. In 2015 he had an internship at NASA's Jet Propulsion Lab in Pasadena, California, USA, where he worked on throw-and-go UAVs in GNSS-denied environments.*

Torleiv H. Bryne *received the M.Sc. and Ph. D. degree in Engineering Cybernetics from the Norwegian University of Science and Technology, Department of Engineering Cybernetics, in 2013 and 2017. He is currently employed as postdoctoral researcher at the same department. His research interests are in the areas of estimation, in particular applied in the context of navigation. UAVs and marine applications are the main focus areas of his research.*

Tor A. Johansen *received the M. Sc. degree in 1989 and the Ph. D. degree in 1994, both in electrical and computer engineering, from the Norwegian University of Science and Technology, Trondheim, Norway. From 1995 to 1997, he worked at SINTEF as a researcher before he was appointed Associated Professor at the Norwegian University of Science and Technology in Trondheim in 1997 and Professor in 2001. He has published several hundred articles in the areas of control, estimation and optimization with applications in the marine, automotive, biomedical and process industries. In 2002 Johansen cofounded the company Marine Cybernetics AS where he was Vice President until 2008. Prof. Johansen received the 2006 Arch T. Colwell Merit Award of the SAE, and is currently a principal researcher within the Center of Excellence on Autonomous Marine Operations and Systems (AMOS) and director of the Unmanned Aerial Vehicle Laboratory at NTNU.*